Scanning diamond NV center magnetometer probe fabricated by laser cutting and focused ion beam milling (F)

Yuta Kainuma,[1,a)] (iD) Kunitaka Hayashi,[1] Chiyaka Tachioka,[1] Mayumi Ito,[2] Toshiharu Makino,[3]
Norikazu Mizuochi,[4] (iD) and Toshu An[1]

AFFILIATIONS

[1]School of Materials Science, Japan Advanced Institute of Science and Technology, Nomi, Ishikawa 923-1292, Japan
[2]Industrial Collaboration Promotion Center, Japan Advanced Institute of Science and Technology, Nomi, Ishikawa 923-1292, Japan
[3]National Institute of Advanced Industrial Science and Technology, Tsukuba, Ibaraki 305-8568, Japan
[4]Institute for Chemical Research, Kyoto University, Gokasho, Uji, Kyoto 611-0011, Japan

[a)]Author to whom correspondence should be addressed: yuta.kaichan@jaist.ac.jp

ABSTRACT

The nitrogen-vacancy (NV) centers in diamond have been applied to scanning magnetometer probes combined with atomic force microscopy (AFM) to demonstrate nanometer-scale magnetic sensing and imaging. However, the scanning diamond NV center probe fabrication requires complicated processes including electron-beam lithography and photolithography. In this study, we introduce an alternative method to fabricate a scanning NV probe using laser cutting and focused ion beam (FIB) milling from a bulk diamond hosting an ensemble of NV centers. A few tens of micrometer-sized diamond pieces, cut by laser processing, were attached to the probe end of a quartz tuning-fork-based AFM. Then, it was fabricated into a few-micrometer-sized diamond NV center probe by using a donut-shaped milling pattern in the FIB processing to avoid damage to the diamond probe surface to degrade the NV$^-$ charged state at the tip apex. By using a home-built scanning NV magnetometer probe microscopy setup, an optically detected magnetic resonance was measured to detect stray magnetic fields demonstrating the imaging of a magnetic structure of approximately 5-μm periodicity from a magnetic tape. This study offers a method with a higher degree of probe-shape control for scanning NV probe that will broaden its application capabilities.

Published under an exclusive license by AIP Publishing. https://doi.org/10.1063/5.0072973

I. INTRODUCTION

With the trend of downsizing of magnetic devices and the introduction of new device concepts in spintronics fields, the detection and imaging of magnetic materials and their spin properties at the nanoscale have gained importance.[1–3] Therefore, the addition of magnetic sensing capabilities to scanning probe microscopy (SPM) techniques such as scanning tunneling microscopy (STM)[4] and atomic force microscopy (AFM)[5] has been developed. To date, scanning magnetometer probes such as spin-polarized STM (SP-STM),[6] magnetic force microscopy (MFM),[7] and scanning superconducting quantum interference device (SQUID) microscopy[8] have been developed. These scanning magnetometer probes using spin-polarized, magnetic, and SQUID scanning probes show imaging of atomically resolved spin structures, magnetic domain structures with a spatial resolution of approximately 10 nm from ferromagnetic samples, and magnetic vortex imaging from superconducting materials with high magnetic-field sensitivity of several nT/$\sqrt{\mathrm{Hz}}$,[8] respectively. However, these have limitations such as the requirement of operation in an ultrahigh vacuum (SP-STM) and low temperature (scanning SQUID microscopy), inability to perform quantitative stray-magnetic field measurements (MFM), and spatial resolution by the size of the magnetic probe and SQUID device.

To overcome these drawbacks, the nitrogen-vacancy (NV) center, a color center in diamond, has gained attention for its magnetic,[9] electric,[10,11] and temperature sensing capabilities[12,13] with nanoscale spatial resolution and high sensitivities, working in various environments.[14–23] The ground spin states of the NV
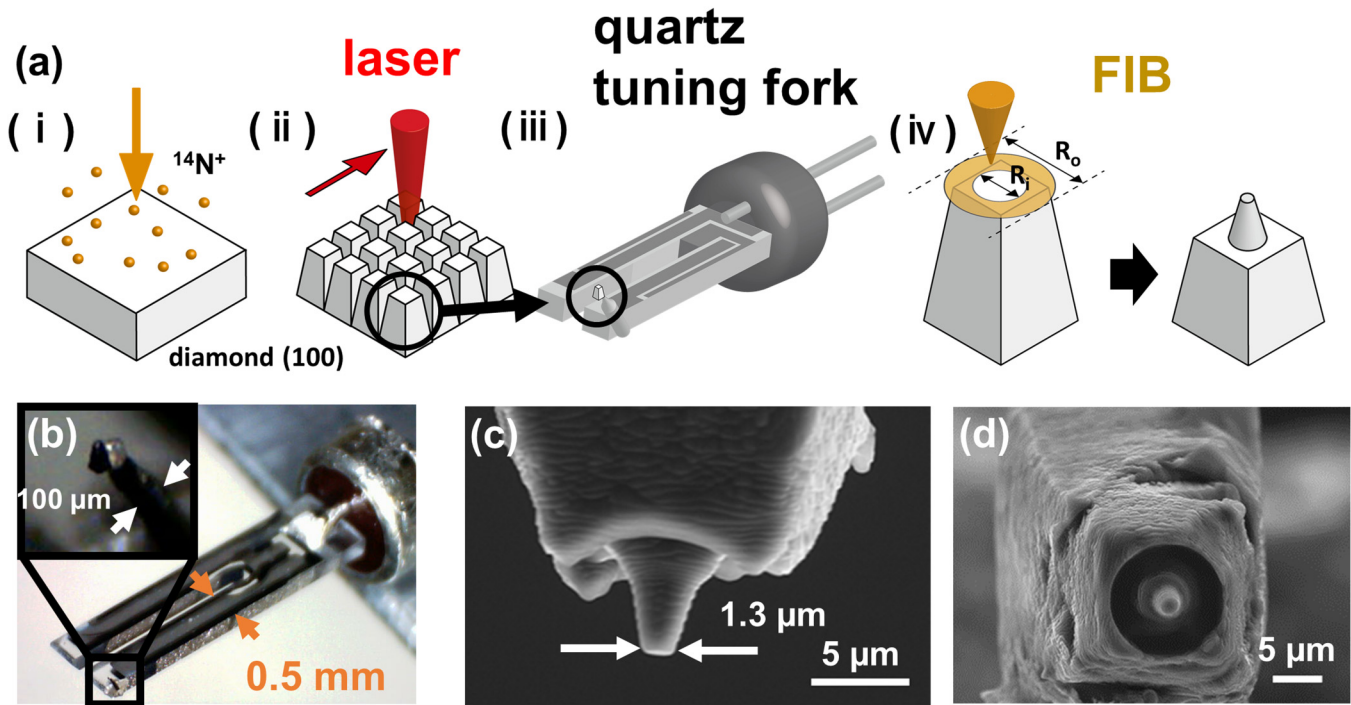
FIG. 1. (a) Illustration of the fabrication procedure of a scanning diamond NV probe: (i) ion implantation with $^{14}N^+$ into the diamond substrate, (ii) laser cutting process of a bulk diamond into rod shapes, (iii) gluing a diamond rod to the apex of a quartz tuning-fork AFM probe, and (iv) the donut-shaped FIB milling process with inner (R_i) and outer (R_o) diameter to fabricate a micropillar. Optical (b) and SEM images of the side view (c) and top view (d) of the scanning diamond NV probe.

center, $m_s = 0$ and $m_s = \pm 1$, can be detected by an optically detected magnetic resonance (ODMR) and stray magnetic fields from a magnetic sample are sensed through the Zeeman effect in the ODMR.[24] By attaching a diamond probe hosting the NV center to an AFM probe end, a scanning NV-center probe for local magnetic imaging can be realized. A magnetic-field sensitivity of $1 \mu T/\sqrt{Hz}$ with an ensemble of NVs probe and a spatial resolution of 3 nm with a single NV probe has been reported depending on the number of NVs with a trade-off relation.[25,26]

The fabrication of NV-hosting diamond probes is key to scanning magnetometer. Recently, the scanning NV diamond probe has become available commercially (Qnami Co., Ltd., QZABRE Co., Ltd.),[26] increasing the number of its users. However, for NV-probe fabrication, it requires photolithography and electron-beam lithography.[27,28] Thus, alternative NV probe fabrication methods are required. This study demonstrates a method for fabricating a scanning diamond NV probe using laser cutting and focused ion beam (FIB) milling, giving a higher degree of control over the probe shape for both the bulk part and the tip, which opens the possibility of optimizing the shape, e.g., to maximize PL collection. FIB has been a powerful tool for fabricating SPM probes milling tip apexes down to a few nanometers;[29,30] however, it cannot be used for scanning NV probe fabrication because of the damage of the diamond structure by Ga^+ ions, which alters the NV^- state to NV^0.[31,32] FIB is used only for cutting the base of the scanning diamond NV

probe[33] and for diamond-hosting NVs at deep positions from surface fabricating solid immersion lenses and photon cavities.[31,34–36] In this study, we demonstrated that a scanning diamond NV probe can be fabricated using a donut-shaped milling pattern in FIB fabrication to avoid NV damage at the probe center position with at least approximately $1 \mu m$ of probe diameter, demonstrating magnetic structure imaging from a magnetic tape.

II. EXPERIMENTAL METHOD

The fabrication procedure for a scanning NV probe with FIB is shown in Fig. 1(a). A (100)-oriented type IIa bulk diamond sample grown by chemical vapor deposition (CVD) was used. To create NV centers, $^{14}N^+$ ions were implanted with a dose of $1.0 \times 10^{12}/cm^2$ with an incident energy of 30 keV followed by annealing at 900 °C for 1 h. The sample was cleaned and oxidized in a solution of a mixture of $HNO_3:H_2SO_4 = 1$ (10 ml):3 (30 ml) at 220 °C for 30 min.

The opposite side of the implanted surface of the bulk diamond was polished to a thickness of $50 \mu m$ and cut into a rod shape of approximately $35 \times 35 \times 50 \mu m^3$ by laser cutting (SYNTEK Co., Ltd.). One rod was removed using a sharp knife and picked up by a chemically etched sharp tungsten wire. The diamond rod was then glued with a silver paste (H20E, EPOTEK Co., Ltd.) to the apex of another chemically etched tungsten wire probe attached to
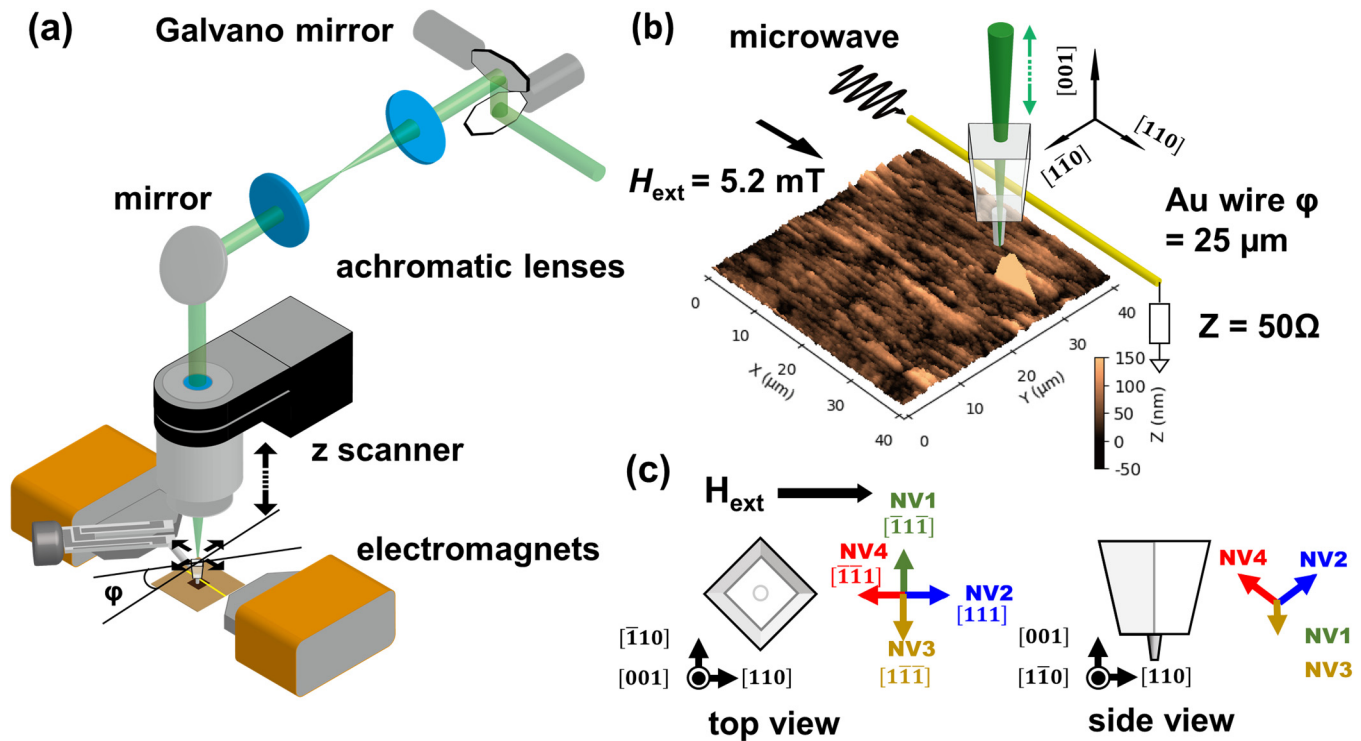
FIG. 2. (a) Experimental configuration combining a confocal scanning laser microscopy with the scanning NV-probe quartz AFM. (b) A 3D topographic AFM image of the magnetic tape sample. A microwave is introduced to the scanning diamond NV probe via Au wire ($\varphi = 25\,\mu m$) overlaid on the sample under an in-plane external magnetic field $H_{ext} = 5.2\,$mT. (c) Side and top views of the quantum axes of NV centers (NV1–NV4) in the diamond probe.

the quartz tuning fork for AFM [Fig. 1(b)]. We note that the used tuning fork (AB38T-32.768kHz, Abracon Co., Ltd.) is relatively large (the effective prong length of 3.3 mm and width of 0.5 mm), and thus a large mass of probes can be attached enabling easy handling and wide application for researchers.

Next, the NV diamond rod front surface was milled by FIB with a 30 kV Ga$^+$ ion source into a probe shape using a donut-shaped milling pattern. Ion implantation by Ga$^+$ ions creates vacancies in a diamond, inducing instability of the NV$^-$ state to NV neutral state[32] can be avoided using a donut-shaped milling pattern. First, FIB milling with inner (R_i: 5.6 μm) and outer (R_o: 23.4 μm) diameters of the donut-shaped milling pattern with an ion-source current of 1.3 μA was used to fabricate a rough shape of the diamond probe. Then, the reduced diameters (R_i: 1.3 μm) and (R_o: 11.9 μm) with an ion current of 730 pA were used for precise fabrication control, which resulted in diameter and length of approximately 1.3 and 6 μm, respectively, of the fabricated diamond probe, as shown in Figs. 1(c) and 1(d).

A home-built confocal scanning microscope system implemented with Galvano mirrors performed optical address and readout of the NV states, as shown in Fig. 2(a). The excitation laser (wavelength: 532 nm) passes through the long working distance (WD) objective lens (TU Plan EPI ELWD, WD: 11 mm, numerical aperture: 0.6, Nikon Co., Ltd.) to excite the NVs attached to the

quartz tuning-fork AFM probe end set between the objective lens and the sample. The vertical focal position was controlled by the z-axis piezo scanner fixed to the objective lens, and the laser was scanned in the horizontal plane by controlling the angle of the Galvano mirrors. An electromagnet was set to apply an in-plane external magnetic field ($H_{ext} = 5.2$ mT) separating energy of electron spin states, $m_s = \pm 1$ of NVs for each quantum axis by the Zeeman effect. The sample was placed on a microstrip line, where an Au wire ($\varphi = 25\,\mu$m) was overlaid on the magnetic tape sample for microwave excitation of NV spin state with 50 Ω termination. A microwave from a signal generator (SG6000F, DS Instruments Co., Ltd.) with a power of 0 dBm, passing through an RF switch (ZYSWA-2-50DR, Mini-Circuits Co., Ltd.) and a circulator (H02S01, Chengdu Bocen Microwave Technology Co., Lid.), was amplified (ZVA-183-S+, Mini-Circuits Co., Ltd.) to 19.3 mW and fed to the Au wire. For the sample, a magnetic tape recorded with an audio signal of 5 kHz shows that an in-plane magnetized magnetic structure of approximately 5 μm, periodicity confirmed by the Bitter method, was used.[37]

The scanning NV diamond probe also works as a quartz tuning fork-based AFM using a resonantly oscillated condition of the phase-locked loop with amplitude-signal feedback for z-distance regulation. When the probe was brought closer to the sample surface, the tuning fork oscillation was horizontal to the
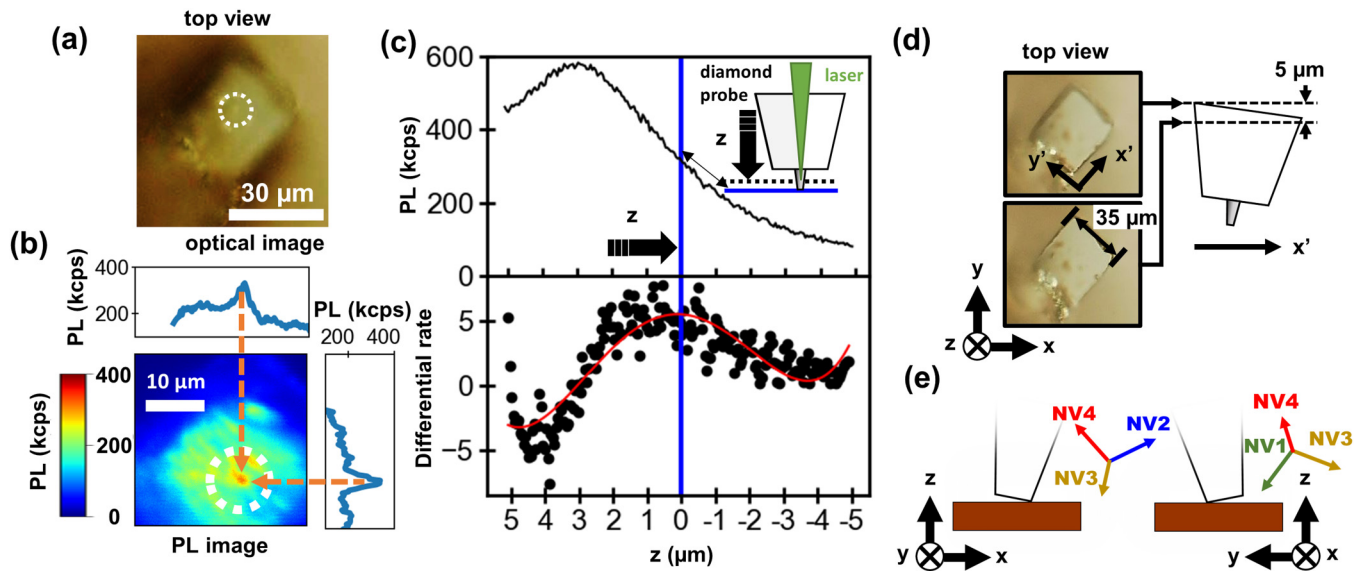
FIG. 3. Optical (a) and PL (b) top-view images of the scanning diamond probe. The probe position was marked by the white dashed circle, where shows maximum PL intensity as shown in the line profiles. (c) PL intensity (solid line) from the NV-diamond probe as a function of the laser-focusing z position. First derivatives of the PL data filtered with Savitzky–Golay (solid circles) and a fitted curve (red solid line) by fourth order polynomial were shown. The fitted-maximum position (blue solid line) was set for tracking of the NV-probe z position. (d) Optical top-view images observed at different focal positions. (e) The relative coordinate of the quantum axis of NVs (NV1–NV4) of the diamond probe tilted to the magnetic sample inferred from (d).

sample plane detecting a frictional force, as shown in Fig. 2(a). The oscillation amplitude used for the quartz tuning fork was calibrated using the vertical oscillation mode setup and was estimated at approximately 35 nm.[38]

The diamond [110] crystal axis of the scanning NV probe is directed parallel to the applied external magnetic field $\mathbf{H}_{ext}$ by adjusting the angle ϕ of the quartz tuning fork, as shown in Figs. 2(a) and 2(b). Figure 2(c) shows a schematic drawing of four possible NV axis orientations in the scanning diamond probe: $[\bar{1}1\bar{1}]$, $[111]$, $[1\bar{1}\bar{1}]$, and $[\bar{1}\bar{1}1]$ shown by green (NV1), blue (NV2), yellow (NV3), and red arrows (NV4), respectively. The vector's inner product of the magnetic field and each NV axis contributes to a resonance frequency shift in the ODMR signal. In the experimental configuration, the ODMR signal from NV1 (NV2) and NV3 (NV4) having a larger angle of nearly 90° (a smaller angle of 35°) to the $\mathbf{H}_{ext}$ direction shows ODMR signals at around the near zero-field splitting frequency of 2.87 GHz (lower and higher resonant frequencies with larger Zeeman splitting).

Figure 3(a) shows an optical top-view image of the scanning diamond-rod probe, where the probe position is indicated by a white dotted circle observed in the experimental configuration in Fig. 2. Figure 3(b) shows the photoluminescence (PL) image obtained from the diamond-rod probe, which shows the maximum PL intensity at the probe position. We note that a high PL intensity background at other areas than the probe is observed, which is due to NVs formation from native impurities of used type IIa diamond. Monitoring the PL intensity, in-plane and z probe positions were tracked using the Galvano mirror and z piezo scanner, respectively,

as shown in Fig. 2(a). The observed PL dependence in the z focal position shows a broad distribution of more than a few micrometers below the probe surface Fig. 3(c). The PL data were differentiated, and the z focal position was set as the maximal z differential rate position to track the vertical position by regulating the z-piezo scanner, as indicated by the blue solid line in Fig. 3(c).[39] This regulated z position is expected to enhance NVs contribution near the surface compared with the z position at the maximum PL.

The scanned NV-diamond probe surface was observed as shown by optical top-view images with different focal positions apart $35\,\mu$m in the y' lateral direction and $5\,\mu$m in the z vertical direction with $\pm 1\,\mu$m uncertainty [Fig. 3(d)], showing tilted angles of approximately 8.1° [arctan (5/35)] to the x' direction with respect to the sample surface, and 11.4° [arctan $(5\sqrt{2}/35)$] to the x and y directions. The tilted probe angle can be adjusted for the final angle within a few degrees by bending two-wire electrodes connected to the tuning fork base [Fig. 1(a) (iii)]. The relative coordinates of the quantum axes of NVs (NV1–NV4) of the diamond probe tilted to the magnetic sample, as inferred from Fig. 3(d), are shown in Fig. 3(e).

III. RESULT AND DISCUSSION

A magnetic tape sample was scanned with a diamond NV center probe with data points of 5×50 corresponding to a scanning range of $5 \times 40\,\mu$m^2 under AFM feedback control. Simultaneously, at each scanning point, the ODMR spectrum measurement was performed with a laser power of 0.84 mW and an input microwave
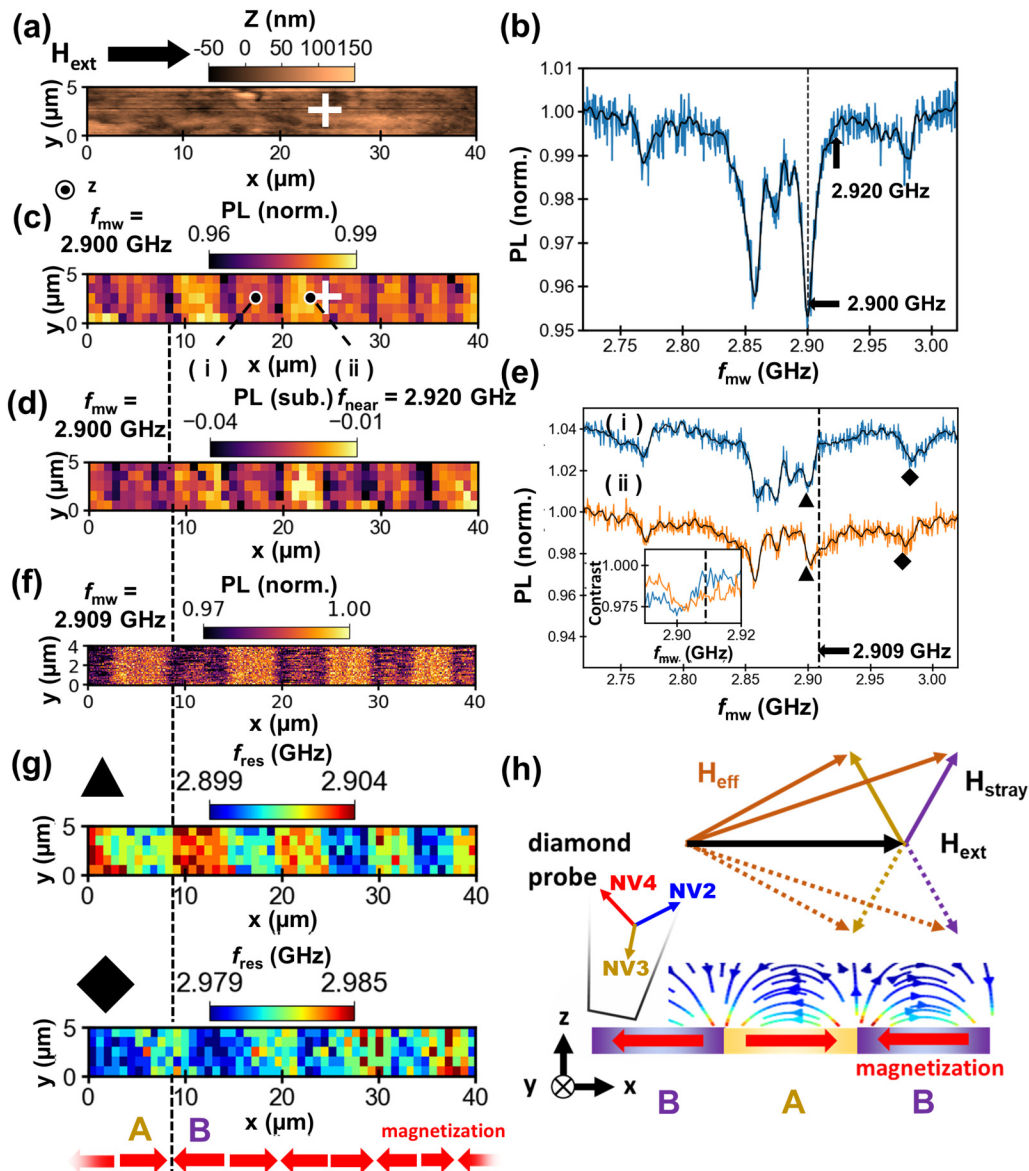
FIG. 4. Imaging of the periodic magnetic domain structure in a magnetic tape using the scanning diamond NV centers probe: an AFM topographic image (a) and an ODMR spectrum (b) measured at the white cross-mark position on the topography of the magnetic tape were shown. The PL intensity at the ODMR frequency of $f_{mw} = 2.900$ GHz indicated with the dashed line in (b) was mapped for each scanning position normalized with averaged background (c) and near-resonant frequency of 2.920 GHz (d) PL intensities. (e) The PL (norm.) intensity of the ODMR spectra obtained at different sample positions of (i) and (ii) indicated in (c) shown with and without offset (inset) zoomed at around a frequency of 2.909 GHz. (f) The PL (norm.) intensities at $f_{mw} = 2.909$ GHz indicated with the dashed line in (e) were mapped for each scanning position. (g) ODMR f_{res} mapping near symbols of the triangle (~2.90 GHz) and rhombus (~2.98 GHz) indicated in (e) for each scanning position. (h) Schematic of magnetic-field imaging by scanning diamond NV probe from the magnetic domain. H_{eff} was shown as a summation of applied in-plane H_{ext} and H_{stray}.

power of 19.3 mW. Figure 4(a) shows an AFM topographic image of the flat magnetic tape with an average roughness of $R_a = 55$ nm. In Fig. 4(b), the ODMR spectrum obtained at the white cross-mark position in Fig. 4(a) was shown, where the PL intensities were normalized by averaged total PL counts [PL (norm.)]. The PL data were smoothed by Savitzky–Golay filter shown by black solid lines. In the spectrum, multiple resonant dips by the Zeeman effect symmetric to the NV's zero-field splitting frequency of 2.87 GHz were observed with the largest ODMR dip signal at 2.900 GHz denoted by the dashed line. (The DC magnetic-field sensitivity was

estimated as $12.3\,\mu\text{T}/\sqrt{\text{Hz}}$ from the resonance-dip slope.) At different scanning NV probe positions, the ODMR resonance frequencies shift according to the spatial variation of the stray magnetic fields resulted in the PL [PL (norm.)] intensity changes at a fixed frequency. Here, PL [PL (norm.)] was normalized by the off-resonant PL intensity of $f_{\text{mw}} = 4.000$ GHz as a reference signal. Subsequently, PL (norm.) at 2.900 GHz is mapped in Fig. 4(c), and a periodic spatial pattern of approximately $5\,\mu\text{m}$ in the x-direction appeared with a dark line at the cross-mark position. Similarly, PL mapping normalized not by averaged total PL intensity but by near resonance PL intensity of $f_{\text{near}} = 2.920$ GHz, which will enhance the contrast twice as shown in Fig. 4(d).[18,19]

In Fig. 4(e), the ODMR spectra, obtained at two different positions labeled by (i) (blue) and (ii) (orange) in Fig. 4(c) on the magnetic tape sample, are shown with offset. These spectra show ODMR frequencies with a slight shift at each scanning position according to the spatial variation of the stray magnetic fields, resulting in PL (norm.) intensity variation at a fixed frequency near resonance, as shown in the inset of Fig. 4(e). In Fig. 4(f), at the near resonance of $f_{\text{mw}} = 2.909$ GHz, PL (norm.) contrast at each scanning position was mapped with a scanning range of $4 \times 40\,\mu\text{m}^2$ (grids of 40×400 points). The obtained PL (norm), intensity mapping image showed a periodic domain pattern corresponding to the magnetic domain structures, where the position (i) and (ii) in Fig. 4(c) are observed as bright and dark domain, respectively, in contrast to Fig. 4(c).

Next, we extracted the resonance-dip frequency (f_{res}) of the ODMR spectra focusing on two resonance dips marked by triangles (approximately 2.90 GHz) and a rhombus (around 2. 98 GHz) in Fig. 4(e). The frequencies of f_{res} at each scanning point are mapped in Fig. 4(g), and a periodic pattern of approximately $10\,\mu\text{m}$ was observed in the mapping of f_{res} (triangle) and f_{res} (rhombus) with a phase shift.

The observed periodic pattern and phase shift can be explained by the relative orientations between the NV axis and the effective magnetic fields: the summation of the external magnetic field and stray magnetic field from the magnetic tape sample. Figure 4(h) shows a schematic drawing of the magnetization vectors of magnetic domains A and B in the magnetic sample together with stray fields from the magnetic domains. The scanning diamond probe on the magnetic sample senses an effective magnetic field ($\mathbf{H}_{\text{eff}}$), which is the summation of the stray magnetic field ($\mathbf{H}_{\text{stray}}$) and the external magnetic field ($\mathbf{H}_{\text{ext}}$).

As shown in Fig. 4(h), the NV1 (NV3) axis in the tilted diamond probe exists nearly in the y–z plane, and the angle between the NV1 (NV3) axis and $\mathbf{H}_{\text{eff}}$ is not perfectly 90°, resulting in small Zeeman splitting to show resonance signal at a lower frequency [triangle in Fig. 4(e)]. When the probe is in the center position of the magnetic domain A (B), $\mathbf{H}_{\text{eff}}$ directed to the x-direction on the surface becomes weaker (stronger) than $\mathbf{H}_{\text{ext}}$. Thus, the NV1 (NV3) axis can sense the change in the x component of $\mathbf{H}_{\text{eff}}$ on the magnetic domains shown in the resonance frequency map of the triangle symbol in Fig. 4(g) with the same-phase periodic pattern, as shown in Figs. 4(c) and 4(f). In contrast, the NV2 (NV4) axis exists nearly within the x–z plane. In this setup, the stray magnetic field at the center of the magnetic domain was roughly estimated from the f_{res} shift, and the angle of the NV2 axis

was approximately $40\,\mu\text{T}$. At a specific magnetic domain boundary position, the NV2 axis and $\mathbf{H}_{\text{eff}}$ become nearly parallel, showing a higher resonance frequency in the resonance frequency map of the rhombus symbol in Fig. 4(g) with a phase-shifted periodic pattern, as shown in Figs. 4(c) and 4(f).

In this study, a diamond probe, with a diameter of approximately $1.3\,\mu\text{m}$ containing roughly 10^3 NVs, was used for the scanning NV-diamond probe fabrication and has a broadening of ODMR from lateral averaging. It is necessary to reduce the probe diameter without damaging the NV^- state at the probe apex, and a single NV hosting probe fabrication is interested in for realizing nanoscale magnetic imaging. For instance, the use of He ion source FIB fabrication having nanoscale fabrication precision is interested in to avoid damage to NV^-.[38] We note that the used tuning-fork AFM oscillation amplitude of 35 nm is relatively large and also causes an ODMR broadening and is required to reduce down to a few nanometers.

Precise analysis of the damage of the diamond probe pillar that will make worse the spin coherence is also important, measuring such as T_1, T_2, stability between NV^0 and NV^- states, strain in the diamond pillar, and effect of Ga atom impurity, in future experiments.[40–42] It was confirmed (not shown here) that the PL intensities from NVs in the diamond pillar measured from the backside through $50\,\mu\text{m}$ thick diamond substrate are reduced to 20% compared with that from the front side. We note that the PL intensities are detected after reduction to half at the half mirror set in the optical line for taking the optical image. The number of NVs in the fabricated probe of about $1\,\mu\text{m}$ diameter can be estimated as roughly 10^3 NVs assuming about 10% of the conversion yield of the implanted nitrogen, and thus the PL count in Fig. 3(c) from the pillar probe of 600 k cps corresponds to 6 k cps/NV. This is one-fifth compared with a single NV count from bulk subsurface (30 k cps) and may come from the damage of NVs in the probe.

For the diamond probe, a type IIa diamond was used, showing the broad asymmetric shape of the ODMR dip signal reflecting a superposition of variations of the stray magnetic field from the magnetic sample surface. This may be because of nitrogen impurities in type IIa diamond other than the implanted nitrogen ions, forming NVs in a broader range of depth during the annealing process, degrading the spatial resolution of magnetic sensing in the vertical and lateral directions (the spatial resolution was confirmed as smaller than 300 nm from a line profile of the magnetic image). This can be improved by using a high-purity diamond sample of electronic grade and shallow nitrogen implantation in a future experiment to refine spatial resolutions.

IV. CONCLUSION

In this study, a fabrication method for a diamond NV center probe for scanning magnetometer was introduced using laser cutting and FIB milling. With a relatively large donut-shaped FIB milling pattern, a diamond probe hosting an ensemble of NV centers was fabricated to avoid damage from the Ga^+ ion source at the center probe position. Stray magnetic fields from the magnetic domain structure of the magnetic tape samples were imaged using a scanning NV magnetometer probe to map the PL intensity at a fixed microwave frequency and the resonance frequencies in the

ODMR spectra. This fabrication method provides a higher degree of probe-shape control of the scanning NV probe, expanding the capabilities of its application.

DATA AVAILABILITY

The data that support the findings of this study are available from the corresponding author upon reasonable request.

REFERENCES

[1] K. Wagner, A. Kákay, K. Schultheiss, A. Henschke, T. Sebastian, and H. Schultheiss, Nat. Nanotechnol. 11, 432 (2016).

[2] Y. Shi, J. Kahn, B. Niu, Z. Fei, B. Sun, X. Cai, B. A. Francisco, D. Wu, Z. X. Shen, X. Xu, D. H. Cobden, and Y. T. Cui, Sci. Adv. 5, eaat8799 (2019).

[3] J. Jersch, V. E. Demidov, H. Fuchs, K. Rott, P. Krzysteczko, J. Münchenberger, G. Reiss, and S. O. Demokritov, Appl. Phys. Lett. 97, 152502 (2010).

[4] G. Binning, H. Rohrer, C. Gerber, and E. Weibel, Phys. Rev. Lett. 49, 57 (1982).

[5] O. Kazakova, R. Puttock, C. Barton, H. Corte-León, M. Jaafar, V. Neu, and A. Asenjo, J. Appl. Phys. 125, 060901 (2019).

[6] R. Wiesendanger, H. J. Ğntherodt, G. Ğntherodt, R. J. Gambino, and R. Ruf, Phys. Rev. Lett. 65, 247 (1990).

[7] Y. Martin and H. K. Wickramasinghe, Appl. Phys. Lett. 50, 1455 (1987).

[8] D. Vasyukov, Y. Anahory, L. Embon, D. Halbertal, J. Cuppens, L. Neeman, A. Finkler, Y. Segev, Y. Myasoedov, M. L. Rappaport, M. E. Huber, and E. Zeldov, Nat. Nanotechnol. 8, 639 (2013).

[9] P. Maletinsky, S. Hong, M. S. Grinolds, B. Hausmann, M. D. Lukin, R. L. Walsworth, M. Loncar, and A. Yacoby, Nat. Nanotechnol. 7, 320 (2012).

[10] F. Dolde, H. Fedder, M. W. Doherty, T. Nöbauer, F. Rempp, G. Balasubramanian, T. Wolf, F. Reinhard, L. C. L. Hollenberg, F. Jelezko, and J. Wrachtrup, Nat. Phys. 7, 459 (2011).

[11] T. Iwasaki, W. Naruki, K. Tahara, T. Makino, H. Kato, M. Ogura, D. Takeuchi, S. Yamasaki, and M. Hatano, ACS Nano 11, 1238 (2017).

[12] K. Hayashi, Y. Matsuzaki, T. Taniguchi, T. Shimo-Oka, I. Nakamura, S. Onoda, T. Ohshima, H. Morishita, M. Fujiwara, S. Saito, and N. Mizuochi, Phys. Rev. Appl. 10, 034009 (2018).

[13] S. Choe, J. Yoon, M. Lee, J. Oh, D. Lee, H. Kang, C. H. Lee, and D. Lee, Curr. Appl. Phys. 18, 1066 (2018).

[14] G. Balasubramanian, I. Y. Chan, R. Kolesov, M. Al-Hmoud, J. Tisler, C. Shin, C. Kim, A. Wojcik, P. R. Hemmer, A. Krueger, T. Hanke, A. Leitenstorfer, R. Bratschitsch, F. Jelezko, and J. Wrachtrup, Nature 455, 648 (2008).

[15] L. Rondin, J. P. Tetienne, P. Spinicelli, C. Dal Savio, K. Karrai, G. Dantelle, A. Thiaville, S. Rohart, J. F. Roch, and V. Jacques, Appl. Phys. Lett. 100, 153118 (2012).

[16] P. Appel, M. Ganzhorn, E. Neu, and P. Maletinsky, New J. Phys. 17, 112001 (2015).

[17] J. P. Tetienne, T. Hingant, L. J. Martínez, S. Rohart, A. Thiaville, L. H. Diez, K. Garcia, J. P. Adam, J. V. Kim, J. F. Roch, I. M. Miron, G. Gaudin, L. Vila, B. Ocker, D. Ravelosona, and V. Jacques, Nat. Commun. 6, 6733 (2015).

[18] L. Rondin, J. P. Tetienne, S. Rohart, A. Thiaville, T. Hingant, P. Spinicelli, J. F. Roch, and V. Jacques, Nat. Commun. 4, 2279 (2013).

[19] J. P. Tetienne, T. Hingant, L. Rondin, S. Rohart, A. Thiaville, E. Jué, G. Gaudin, J. F. Roch, and V. Jacques, J. Appl. Phys. 115, 17D501 (2014).

[20] I. Gross, L. J. Martínez, J. P. Tetienne, T. Hingant, J. F. Roch, K. Garcia, R. Soucaille, J. P. Adam, J. V. Kim, S. Rohart, A. Thiaville, J. Torrejon, M. Hayashi, and V. Jacques, Phys. Rev. B 94, 064413 (2016).

[21] J. P. Tetienne, A. Lombard, D. A. Simpson, C. Ritchie, J. Lu, P. Mulvaney, and L. C. L. Hollenberg, Nano Lett. 16, 326 (2016).

[22] L. Thiel, Z. Wang, M. A. Tschudin, D. Rohner, I. Gutiérrez-Lezama, N. Ubrig, M. Gibertini, E. Giannini, A. F. Morpurgo, and P. Maletinsky, Science 364, 973 (2019).

[23] T. X. Zhou, J. J. Carmiggelt, L. M. Gächter, I. Esterlis, D. Sels, R. J. Stöhr, C. Du, D. Fernandez, J. F. Rodriguez-Nieva, F. Büttner, E. Demler, and A. Yacoby, Proc. Natl. Acad. Sci. U.S.A. 118, e2019473118 (2021).

[24] A. Gruber, A. Dräbenstedt, C. Tietz, L. Fleury, J. Wrachtrup, and C. Von Borczyskowski, Science 276, 2012 (1997).

[25] L. Rondin, J. P. Tetienne, T. Hingant, J. F. Roch, P. Maletinsky, and V. Jacques, Rep. Prog. Phys. 77, 056503 (2014).

[26] See https://qnami.ch/ for Qnami and https://qzabre.com/ for QZABRE.

[27] P. Appel, E. Neu, M. Ganzhorn, A. Barfuss, M. Batzer, M. Gratz, A. Tschöpe, and P. Maletinsky, Rev. Sci. Instrum. 87, 063703 (2016).

[28] T. X. Zhou, R. J. Stöhr, and A. Yacoby, Appl. Phys. Lett. 111, 163103 (2017).

[29] B. G. Konoplev, O. A. Ageev, V. A. Smirnov, A. S. Kolomiitsev, and N. I. Serbu, Russ. Microelectron. 41, 41 (2012).

[30] K. Akiyama, T. Eguchi, T. An, Y. Fujikawa, Y. Yamada-Takamura, T. Sakurai, and Y. Hasegawa, Rev. Sci. Instrum. 76, 033705 (2005).

[31] I. Bayn, B. Meyler, J. Salzman, and R. Kalish, New J. Phys. 13, 025018 (2011).

[32] C. Santori, P. E. Barclay, K. M. C. Fu, and R. G. Beausoleil, Phys. Rev. B 79, 125313 (2009).

[33] J. Kleinlein, T. Borzenko, F. Münzhuber, J. Brehm, T. Kiessling, and L. W. Molenkamp, Microelectron. Eng. 159, 70 (2016).

[34] L. Marseglia, J. P. Hadden, A. C. Stanley-Clarke, J. P. Harrison, B. Patton, Y. L. D. Ho, B. Naydenov, F. Jelezko, J. Meijer, P. R. Dolan, J. M. Smith, J. G. Rarity, and J. L. O'brien, Appl. Phys. Lett. 98, 189902 (2011).

[35] Q. Jiang, D. Liu, G. Liu, Y. Chang, W. Li, X. Pan, and C. Gu, J. Appl. Phys. 116, 044308 (2014).

[36] T. Jung, L. Kreiner, C. Pauly, F. Mücklich, A. M. Edmonds, M. Markham, and C. Becher, Phys. Status Solidi Appl. Mater. Sci. 213, 3254 (2016).

[37] F. Bitter, Phys. Rev. 38, 1903 (1931).

[38] T. An, T. Nishio, T. Eguchi, M. Ono, A. Nomura, K. Akiyama, and Y. Hasegawa, Rev. Sci. Instrum. 79, 033703 (2008).

[39] Y. Wang, Z. Zhao, Z. Chen, L. Zhang, K. Kang, and J. Deng, Appl. Opt. 50, 6452 (2011).

[40] L. Hacquebard and L. Childress, Phys. Rev. A 97, 063408 (2018).

[41] B. J. Shields, Q. P. Unterreithmeier, N. P. De Leon, H. Park, and M. D. Lukin, Phys. Rev. Lett. 114, 136402 (2015).

[42] S. Bolshedvorskii, S. Bogdanov, A. Zeleneev, V. Soshenko, O. Rubinas, D. Radishev, M. Lobaev, A. Vikharev, A. Gorbachev, A. Smolyaninov, V. Sorokin, and A. Akimov, AIP Conf. Proc. 2241, 020005 (2020).